Isı Bilimi ve Tekniği Dergisi, 42, 141-156, 2022
J. of Thermal Science and Technology

ISSN 1300-3615
https://doi.org/10.47480/isibted.1107492

FAST AND PREDICTIVE HEAT PIPE DESIGN AND ANALYSIS TOOLBOX: H-PAT

Samet SAYGAN[a*], Yigit AKKUS[a], Zafer DURSUNKAYA[b***] and Barbaros ÇETİN[c****]**
[a]ASELSAN Inc., 06200 Yenimahalle, Ankara, Turkey
[b]Department of Mechanical Engineering, Middle East Technical University, 06800 Çankaya, Ankara, Turkey
[c]Mechanical Engineering Department, I.D. Bilkent University, 06800 Çankaya, Ankara, Turkey
*ssaygan@aselsan.com.tr, ORCID: 0000-0002-8392-6292
**yakkus@aselsan.com.tr, ORCID: 0000-0001-8978-3934
***refaz@metu.edu.tr, ORCID: 0000-0003-3711-0361
****barbaros.cetin@bilkent.edu.tr, ORCID: 0000-0001-9824-4000

(Geliş Tarihi: 28.12.2021, Kabul Tarihi: 12.04.2022)

Abstract: For the assessment of the thermal performance of heat pipes, a wide range of modeling is available in the literature, ranging from simple capillary limit analyses to comprehensive 3D models. While simplistic models may result in less accurate predictions of heat transfer and operating temperatures, comprehensive models may be computationally expensive. In this study, a universal computational framework is developed for a fast but sufficiently accurate modeling of traditional heat pipes, and an analysis tool based on this framework, named Heat Pipe Analysis Toolbox, in short H-PAT is presented. As a diagnostic tool, H-PAT can predict the fluid flow and heat transfer from a heat pipe under varying heat inputs up to the onset of dryout. During the initial estimation of phase change rates, the solutions of particular thin film phase change models are avoided by specifying an appropriate pattern for the mass flow rate of the liquid along the heat pipe rather than using finite element/volume based methods for the computational domain. With the help of a modular structure, H-PAT can simulate heat pipes with different wick structures as long as an expression for the average liquid velocity and corresponding pressure drop can be introduced. H-PAT is also capable of analyzing heat pipes with variable cross-sections, favorable/unfavorable gravity conditions and utilizes temperature dependent thermo-physical properties at evaporator, condenser and adiabatic regions together with heat input sensitive vapor pressure. In addition, H-PAT performs the computation very fast which also makes it a perfect design tool for researchers and design engineers in the field of thermal management.
Keywords: Heat pipe modeling, flat-grooved heat pipes, phase-change modeling, H-PAT

HIZLI VE ÖNGÖRÜLÜ ISI BORUSU TASARIM VE ANALİZ ARACI: H-PAT

Özet: Isı borularının termal performansının değerlendirilmesi için, literatürde basit kılcal limit analizlerinden kapsamlı 3D modellere kadar geniş bir modelleme yelpazesi mevcuttur. Basit modeller, ısı transferi ve çalışma sıcaklıklarının daha düşük doğrulukla tahmin ederken, kapsamlı modeller hesaplama açısından yük getirmektedir. Bu çalışmada, geleneksel ısı borularının hızlı fakat yeterince doğru bir şekilde modellenmesi için evrensel bir hesaplama yöntemi geliştirilmiş ve bu yönteme dayalı olarak Isı Borusu Analizi Araç Aracı, kısaca H-PAT olarak adlandırılan bir analiz aracı sunulmuştur. Bir tanı aracı olarak H-PAT, kuruma başlangıcına kadar değişen ısı girdileri altında bir ısı borusundan sıvı akışını ve ısı transferini tahmin edebilir. Faz değişim hızlarının ilk tahmini sırasında, hesaplama alanı için sonlu eleman/hacim tabanlı yöntemler kullanmak yerine, ısı borusu boyunca sıvının kütle akış hızı için uygun bir model belirlenerek belirli ince film faz değişim modellerinin çözümlerinden kaçınılır. Modüler bir yapının yardımıyla, H-PAT, ortalama sıvı hızı ve buna karşılık gelen basınç düşüşü için bir formülasyon sunulabildiği sürece farklı fitil yapılarına sahip ısı borularını simüle edebilir. H-PAT ayrıca değişken kesitli ısı borularını, yerçekiminin pozitif/negatif yönde etki ettiği koşullarını da analiz etme yeteneğine sahiptir ve ısı girdisine duyarlı buhar basıncı ile evaporatör, kondenser ve adyabatik bölgelerde sıcaklığa bağlı termo-fiziksel özellikleri kullanır. Buna ek olarak, H-PAT hesaplamayı çok hızlı gerçekleştirir ve bu da onu termal yönetim alanındaki araştırmacılar ve tasarım mühendisleri için mükemmel bir tasarım aracı haline getirir.
Anahtar Kelimeler: Isı borusu modellemesi, düz oluklu ısı borusu, faz değişimi modellenmesi, H-PAT.

NOMENCLATURE

Symbols

g	gravitational acceleration [m/s^2]
$\mathbb{G}(z)$	geometric function
h	height [m]
h_{fg}	latent heat of evaporation [J/kg]
k	thermal conductivity [W/m·K]
L	length [m]
M	molar mass of liquid [kg/mol]
$\dot{m}$	mass flow rate [kg/s]
$\mathbf{n}$	unit vector in normal direction
P	pressure [Pa]
$\dot{q}$	heat transfer rate [W]
$\mathcal{R}$	meniscus radius of curvature [m]
R	thermal resistance [K/W]
R_u	universal gas constant [J/mol·K]
T	temperature [K]
U	velocity [m/s]
V	volume [m^3]
w	width [m]

Greek Symbols

$\hat{\sigma}$	accommodation coefficient
δ	liquid film thickness [m]
ε	convergence criterion
θ	contact angle [rad]
ρ	density [kg/m^3]
μ	dynamic viscosity [Pa·s]
ν	kinematic viscosity [m^2/s]
σ	surface tension [N/m]
Δ	delta

Subscripts

a	adiabatic
ax	axial
b	base
c	condenser
$cond$	conduction
e	evaporation
f	fin
ft	fin top
g	groove
gf	groove film
l	liquid
m	mean
$p.c.$	phase change
s	solid
tf	thin film
tot	total
v	vapor

INTRODUCTION

Thermal management of electronics has always been an essential part of device design to secure operation without any thermal damage or performance degradation. Today, this is of utmost importance for high density electronics since the peak power density of modern chip technology is limited by the heat spreading ability of the thermal architecture. The key factor in the removal of hot spots in high heat flux electronics is the minimization of thermal resistance of the path whereby the waste heat is conveyed to the heat sink. When the heat is transported through a solid media, thermal resistance is dictated by its thermal conductivity, a material property with a modest upper limit. This barrier, on the other hand, can be overcome by heat spreaders utilizing the liquid-vapor phase change mechanism to transport the energy. As the most prevalent, heat pipes have been serving thermal engineers for more than half a century (Grover *et al.*, 1964) in both terrestrial and space applications (Faghri, 1995; Reay *et al.*, 2013), in most cases without an alternative.

Heat pipe is a sealed container, in which liquid and vapor phases of a pure substance, the working fluid, continuously circulate to sustain the phase change heat transfer. Various types of heat pipes based on the routes of the phases exist, such as traditional heat pipes (cross flow of the phases along the same axis), loop heat pipes (different paths for the two phases) and pulsating heat pipes (conjugate flow of the phases along the same direction). Heat pipes can be manufactured in various geometrical shapes (Reay *et al.*, 2013) and their size can range from nanometers to meters (Hoa *et al.*, 2003; Peterson *et al.*, 1993; Akkus *et al.*, 2019). Regardless of their type, shape or size, all heat pipes share the same working principle: passive transport of the working fluid triggered by continuous phase change.

Capillary structures positioned at the inner wall of a heat pipe (called the wick) are responsible for the transportation of the liquid from the condenser to the evaporator. Whilst wick structures are generally made of porous material or parallel grooves, some heat pipes with sharp-angled corners (generally called micro heat pipes) utilize the inner corners as liquid arteries without a need for an additional wick structure. Since the amount of energy transferred via phase change is proportional to the amount of liquid transport, the ultimate objective is to maximize mass transfer through the wick, yet this is restricted by the capillary limit. A proper estimation of the capillary limit requires writing a balance between the surface, body and pressure forces for flow modeling, which is not straightforward due the complexity of solving the inherently non-linear flow equations. Introducing several simplifying assumptions is inevitable in order to obtain a solution to the flow.

In the case of a porous wick, a common approach in the literature (Vafai and Wang, 1992; Aghvami and Faghri, 2011; Ferrandi *et al.*, 2013; Kolliyil *et al.*, 2020) is to apply Darcy's law, which, however, neglects the boundary, inertial and variable porosity effects (Vafai, 1984). As a result, several modifications were suggested for Darcy's law in the literature. Following the analysis reported in (Vafai and Tien, 1981), non-Darcian transport of liquid was considered in (Zhu and Vafai, 1996; Zhu and Vafai, 1999) by incorporating the boundary and inertial effects. Inclusion of gravity as a body force into the Darcy's equation was also attempted (Zhu and Vafai, 1996; Anand *et al.*, 2008).

Due to the ease of controllable manufacturing and developing associated numerical and analytical solutions, grooved and micro heat pipes have been widely studied in the literature (Babin *et al.*, 1990; Kim *et al.*, 2008; Do *et al.*, 2008; Alijani *et al.*, 2018; Alijani *et al.*, 2019). In the case of flow in open channels, gradually changing flow area does not lead to a sudden acceleration or deceleration of the liquid enabling the omission of inertial and boundary effects. This results in a force balance between the Laplace pressure originating from the curvature change of liquid-vapor interface, viscous losses and gravity, which is in general, more effective in grooved heat pipes compared to the ones with a porous wick (Reay *et al.*, 2013; Atay *et al.*, 2019). Counter flow of vapor and liquid results in viscous losses due to shear stresses between liquid-wall, vapor-wall and liquid-vapor at the interface. While the amount of mass transported through the adiabatic region remains nearly constant, the main change is along the evaporator and condenser regions; consequently, additional models (Akkus and Dursunkaya, 2016; Akdag *et al.*, 2020) to account for phase change rates along the evaporator and condenser sections should be employed. When all of these effects are considered, the solution approach is to numerically solve the mass and momentum balance equations in both domains together with the Young-Laplace equation (Do *et al.*, 2008; Lefèvre *et al.*, 2008; Odabasi, 2014). One basic simplification is to estimate the variation of phase change rates along the evaporator and the condenser. Linear variation of the phase change was assumed (Anand *et al.*, 2008; Kim *et al.*, 2003; Chen *et al.*, 2009; Desai *et al.*, 2019; Singh, 2020) and confirmed (Aghvami and Faghri, 2011; Odabasi, 2014) in previous studies. Similarly, the assumption of uniform heat flux in these regions also eliminated the need for phase change models (Lips *et al.*, 2011). On the other hand, the most common assumption in flow modeling is the decoupling of phase change and axial liquid flow by assuming the liquid flow between the mid-planes of the condenser and the evaporator (Faghri, 1995; Reay *et al.*, 2013; Jiang *et al.*, 2014; Ömür *et al.*, 2018). However, this approach may lead to substantial errors in the modeling of heat pipes with short or no adiabatic sections.

Despite the presupposition of the phase change mass transfer variation, the flow problem still remains complex due to the alteration of both liquid and vapor pressures, which are coupled via the Young-Laplace equation throughout the flow domain. Momentum balance in both domains with the Young-Laplace equation form a set of ordinary differential equations, which was solved by numerical methods (such as Runga-Kutta) in previous studies (Anand *et al.*, 2008; Kim *et al.*, 2003). An analytical solution, on the other hand, is viable when the vapor pressure variation is not taken into consideration in the Young-Laplace equation. In this case, liquid pressure distribution can be obtained by integrating the momentum equation and the Young-Laplace equation can be employed to calculate the distribution of the interfacial curvature. In fact, capillary limit analyses in well-known textbooks (Faghri, 1995; Reay *et al.*, 2013; Jiang *et al.*, 2014; Peterson, 1994) also rely on the assumption of a constant vapor pressure, which can be the saturation pressure at the average working temperature of the heat pipe. However, these analyses still accounted for the vapor pressure loss by employing correlations for the vapor pressure drop (Reay *et al.*, 2013; Chi, 1976; Faghri, 1989). In certain cases such as short adiabatic region or low Reynolds number, the omission of liquid-vapor shear (Lefèvre *et al.*, 2008) and vapor pressure loss (Suman *et al.*, 2005) were also suggested, which further simplifies the problem and aids in finding analytical solutions.

Even after the aforementioned simplifications, finding analytical solutions to the momentum equation of the liquid is still challenging due to the presence of free surface boundaries such as menisci attached to groove edges in grooved heat pipes or those in the corner regions of micro heat pipes. Therefore, suitable correlations have been employed to relate the pressure gradient with an average flow velocity or mass flow rate. The crudest approach is to utilize Darcy's law, derived for a circular groove with a suitable effective flow diameter (Reay *et al.*, 2013). A better approach is to employ a cross-section specific permeability in terms of a non-dimensional parameter, the Poiseuille number, which can be viewed as a friction factor and is commonly expressed by Shah and London correlation (Faghri, 1995). However, a correction is necessary to include the effect of liquid-vapor interaction at the interfacial boundary (Kim *et al.*, 2003). Schneider and DeVos, 1980 suggested a modification to the Poiseuille number to account for the interfacial shear, and many subsequent studies (Anand *et al.*, 2008; Do *et al.*, 2003; Ömür *et al.*, 2018; Khrustalev *et al.*, 1995) adopted this approach to calculate the viscous losses at liquid-wall and liquid-vapor boundaries. Instead of utilizing shear stress correlations, direct analytical solution of momentum equation for vapor and/or liquid phases was also suggested by solving Poisson's equation or assuming parabolic velocity distribution in the literature (Zhu and Vafai, 1999; Chen *et al.*, 2009).

Modeling the fluid flow, thereby estimating the capillary limit is crucial, but not adequate for the assessment of the overall performance of a heat pipe due to several reasons. First of all, some portion of the heat load is inevitably transferred by the conduction in the axial direction through the container walls. The ratio of the heat transfer rate via phase change to the conduction heat transfer, which can be viewed as an effectiveness parameter (Akkus *et al.*, 2019; Alijani *et al.*, 2018), should be high to ensure the proper functioning of the heat pipe. Therefore, axial conduction should be incorporated in the modeling. Moreover, depending on the heat input, the amount of liquid and vapor changes considerably along the heat pipe. The accumulation of the liquid in the condenser, referred to as liquid block/pool or flooded region (Ki *et al.*, 2003; Do *et al.*, 2008; Alijani *et al.*, 2019; Chen *et al.*, 2009; Desai *et al.*, 2019), affects not only the effective flow length but also the thermal resistance along both longitudinal and vertical directions

(Do *et al.*, 2008). Furthermore, the axial distribution of temperature directly affects the thermal properties of the fluid along the heat pipe. Thus, the effective thermal resistance of a heat pipe may change across varying heat inputs (Li *et al.*, 2015; Khalili and Shafii, 2016). As a result, thermal modeling is inherently coupled to the flow modeling, and they should be solved simultaneously, which requires an iterative solution approach. In the literature, in addition to the studies considering phase change as the sole energy transport mechanism (Babin *et al.*, 1990; Chen *et al.*, 2009; Singh, 2020; Suman *et al.*, 2005; Khrustalev and Faghri, 1995; Khrustalev and Faghri, 1994; Longtin *et al.*, 1994; Rullière *et al.*, 2007), uni-directional (Do *et al.*, 2008; Hung and Tio, 2010; Hung and Tio, 2012; Chang and Hung, 2014; Tio and Hung, 2015; Jafari *et al.*, 2020) and multidirectional (Kim *et al.*, 2003; Lefèvre *et al.*, 2008; Desai *et al.*, 2019; Lips *et al.*, 2011; Catton and Yao, 2016) thermal resistance networks were implemented to model the heat transfer in a heat pipe.

In summary, a massive body of literature exists for heat pipe modeling from simple capillary limit analyses (Faghri, 1995; Reay *et al.*, 2013; Peterson, 1994) to the comprehensive 3D models (Do *et al.*, 2008; Lefèvre *et al.*, 2008). While simplistic models may fail to capture the flow domain properly, thereby result in inaccurate predictions for the heat transfer; comprehensive models are computationally expensive demanding long computation times. The objective of the current study is to draw a universal computational framework for a fast but sufficiently accurate modeling of traditional heat pipes and to develop an associated analysis tool named Heat Pipe Analysis Toolbox, in short H-PAT, which is also available as a MATLAB Toolbox for academic use. H-PAT is capable of diagnosing the operation of a heat pipe working under varying heat inputs up to the onset of dryout. It targets to find an accurate liquid distribution along the wick (including liquid pool if present) based on the available analytical solutions and/or correlations for the liquid ow, then establishing the corresponding 3D thermal resistance network, which is composed of evaporator, condenser and adiabatic region resistances. During the initial estimation of phase change rates, the solutions of particular thin film phase change models are avoided by specifying an appropriate pattern for the mass flow rate of the liquid along the heat pipe rather than using finite element method for the computational domain. Modular structure of H-PAT enables handling heat pipes with different wick structures as long as an expression can be introduced for the average liquid velocity. H-PAT is also able to analyze heat pipes with varying cross-sections, favorable/unfavorable gravity conditions and utilizes temperature dependent thermo-physical properties at the evaporator, condenser and adiabatic regions together with heat input sensitive vapor pressure, which makes the tool distinctive.

The paper is organized as follows: in Section 2, computational scheme and modeling strategies in flow and thermal models of H-PAT are introduced. In Section 3, H-PAT is validated with benchmark simulations for rectangular grooves with both constant and variable cross-sections along the heat pipe. Concluding remarks are provided in Section 4.

MODELING FRAMEWORK

Heat pipe modeling requires solving the fluid flow and heat transfer. While the former basically determines the overall mass flow rate and the amount of phase change heat transfer thereof, the latter is linked to the overall temperature distribution along the heat pipe. In fact, these two are strongly coupled due to the conjugate heat and mass transfer, especially when the phase change mechanism is considered. Moreover, temperature dependence of thermo-physical properties affects the results to a certain extent. Thus, the fluid flow and heat transfer should be simultaneously considered in modeling, which can be accomplished by implementing an iterative solution approach. In this section, first, the details of flow model and thermal model are provided, then the iterative solution procedure is presented.

Flow Model

Flow model considers only the liquid flow based on the assumption of negligible shear stress associated with the liquid-vapor interaction. The model adopts an analytical approach for the solution of the liquid flow. A relation between mass flow rate of the liquid and the pressure variation along the heat pipe should be defined to find the pressure distribution. Therefore, a geometrical function, $\mathbb{G}(z)$, which depends on the type and geometry of the wick structure, can be defined. Liquid flow along the heat pipe axis is sustained by the pressure gradient in the same direction. If the analytical solution of the liquid velocity is available over the cross-sectional flow area, then the pressure gradient term appears in the solution. Mass flow rate can be calculated by integrating the velocity distribution and mass flow rate along the heat pipe axis, and expressed as the product of the pressure gradient and the resultant function following the integration as:

$$\dot{m}_l(z) = \int (\rho \boldsymbol{u}) \cdot \boldsymbol{n}\, dA = \mathbb{G}(z)\left(\frac{dp}{dz} + f_b\right) \qquad (2.1)$$

where ρ and f_b are the liquid density and the constant associated with a body force, respectively. The equation for pressure distribution in the liquid is obtained by integrating the prediction for mass flow rate variation along the heat pipe as:

$$p(z) = \int \left(\frac{\dot{m}_l}{\mathbb{G}(z)} - f_b\right) dz, \quad 0 \le z \le L^{eff} \qquad (2.2)$$

where L^{eff} is the effective axial flow length of the liquid. Boundary conditions for the liquid pressure required for the integration in Eq. (2.2) are directly linked to the assumptions on the operation of the heat pipe. A proper operation should be free from the occurrence of dryout in the evaporator. The onset of dryout can be determined

based on the angle at the triple line, where three phases (solid walls of the wick and liquid and vapor phases of the working fluid) meet. This angle can decrease up to the *contact angle*, θ_{ca}, a characteristic property of a liquid in contact with a certain solid surface. Further stretching of the liquid beyond the contact angle may result in sudden occurrence of dryout (Nilson *et al.*, 2006). Therefore, the pressure value at the evaporator end of the heat pipe ($z = 0$) is calculated based on the contact angle using Young-Laplace relation (Eq. 2.3a). At the opposite side of the heat pipe, pressure gradient vanishes at the point where the axial liquid flow ceases ($z = L^{eff}$). This point is the physical end boundary of the heat pipe if there is no pool region at the condenser, whereas, when the pool region is present, the point corresponds to the starting point of the flooded region since there is no considerable axial flow along the liquid pool. In accordance with these discussions, the boundary conditions can be summarized as:

$$p(z=0) - p_v = -\sigma\left(\frac{1}{\mathcal{R}_1} + \frac{1}{\mathcal{R}_2}\right) \tag{2.3a}$$

$$\left(\frac{dp}{dz}\right)_{z=L^{eff}} = 0 \tag{2.3b}$$

where p_v and σ are vapor pressure and surface tension, respectively. $\mathcal{R}_1$ and $\mathcal{R}_2$ are radii of curvature of the free surface in principal directions. The mass flow rate of the liquid, $\dot{m}_l$, along the heat pipe can be approximated to change linearly in evaporator and condenser regions considering the predictions of prior works (Odabasi, 2014; Chen *et al.*, 2009; Rullière *et al.*, 2007; Hung and Tio, 2012; Elnaggar *et al.*, 2012; Huang and Chen, 2017), while the axial liquid flow rate remains approximately constant in the adiabatic region due to negligible phase change. To this effect, $\dot{m}_l$ can be expressed as a linear function of the axial coordinate, z, in the evaporator and condenser. However, this approach is not accurate due to presence of axial conduction in the solid, and in general, will not yield smooth transitions between the evaporator/condenser regions in the adiabatic zone. By the inclusion of axial conduction in the analysis and solving the axial domain with fine increments resolves this handicap. Therefore, the liquid domain is divided into a number of slices in each region accordingly. Inside each slice, the mass flow rate of liquid is approximated as a linear function of $z, i.e. \dot{m}_{l,i} = d_{0,i} + d_{1,i} z_i$, where subscript i designates the corresponding slice. The implementation of multiple slices in the numerical modeling introduces additional boundaries in between, where flow continuity serves as the boundary condition for each slice as follows:

$$\left(\frac{dp}{dz}\right)_i = \frac{\dot{m}_i}{\mathbb{G}(z_i)} \tag{2.3c}$$

where $\dot{m}_i$ is the flow rate at the intersection of the slices. At the first iterative step, its value is assigned based on initially estimation of the distribution of total liquid flow along the heat pipe. In the following iterations, the predictions of the previous iteration are employed.

The flow model is valid for different types of wick structures or geometries. Each wick structure yields a specific geometrical function $\mathbb{G}(z)$. Two versatile wick structures are grooved and sintered wicks. While the former is primarily investigated in the current study, the extension of the current modeling for the latter is provided in Appendix B by summarizing the corresponding equations. Regardless of the geometry, the capillary pressure associated with the varying topology of the free surface drives the liquid flow, whereas viscous forces due to the friction of the liquid with the walls oppose it. Consequently, the force balance is established between viscous and pressure forces similar to Poiseuille flow in channels and the linear momentum equation in the axial direction becomes Poisson's equation. To enable the utilization of an available solution to this equation, open channel (groove) flow is treated as the half-domain flow in rectangular duct of width w and height $2h$. Then, the separation of variables is used to solve Poisson's equation with homogeneous Dirichlet boundary conditions. Finally, the mean velocity, U_m, is determined by integrating the velocity distribution over the cross-section as:

$$U_m = \frac{16}{(wh)^2}\frac{\Delta P}{\mu L^{eff}}\sum_{m=1}^{\infty}\sum_{n=1}^{\infty}\frac{1}{(\beta_m^2 + \lambda_n^2)\beta_m^2\lambda_n^2} \tag{2.4}$$

where μ is the dynamic viscosity of the liquid, $\lambda_n = (2n-1)\pi/w$ and $\beta_m = (2m-1)\pi/2h$. The convergence of the series in Eq. 2.4 is fast; therefore, the leading term gives a sufficiently accurate approximation. Mass flow rate inside the groove can be determined by multiplying the mean velocity with density and half cross-sectional area of the rectangular duct. This approach induces a restricted deviation when meniscus is near at, i.e. the edge angle between meniscus and wall, θ, is around 90°, because of the slight deformation of the meniscus with respect to the total cross-sectional area of the liquid. However, the meniscus deformation becomes non-negligible near the evaporator end of the heat pipe; therefore, a correction factor, $\Gamma(\theta)$, based on the ratio of deformation area to total cross-sectional area is applied in the calculation of mass flow rate. Finally, the geometrical function, $\mathbb{G}(z)$, for the rectangular groove is obtained as:

$$\mathbb{G}(z) = \Gamma\frac{256}{\nu\pi^6}\frac{w^3(z)h^3(z)}{[w^2(z) + 4h^2(z)]} \tag{2.5}$$

where ν is the kinematic viscosity of the liquid. The width and height of the groove are written as a function of z, which enables the calculation of pressure variation in both constant and variable cross-sections in the rectangular grooved heat pipes. The extension of the flow model for sintered wicks is provided in Appendix B.

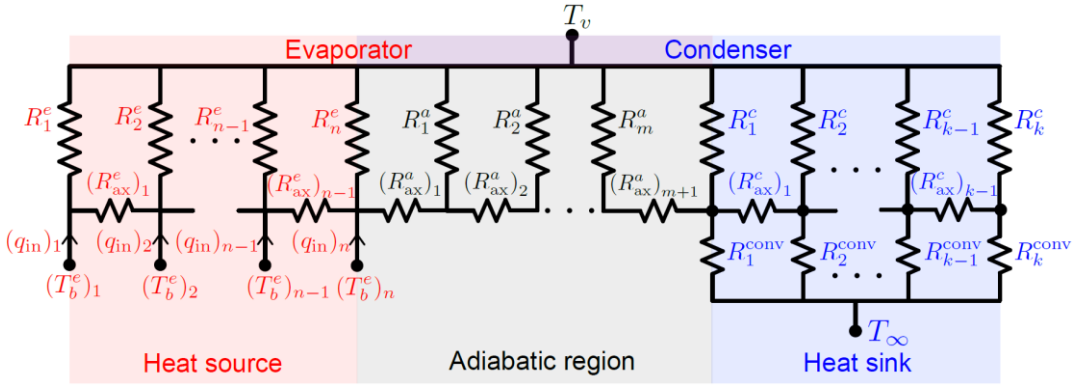

Figure 1. Schematic representation of the thermal resistance model. Heat source and heat sink indicate the outside surface of the heat pipe, where the heat load is applied and removed, respectively. Adiabatic region is the zone exposed to the exterior with no heat input or output. The evaporator and condenser stand for the internal zones, where evaporation and condensation takes place, respectively. T_v and T_∞ are the internal vapor and external coolant temperatures, respectively. There are n, m, and k numbers of slices for the heat source, adiabatic, and heat sink regions, respectively

Thermal Model

The thermal model establishes a thermal resistance network to simulate the heat transfer through a heat pipe. Similar to the approach adopted in the flow model, the thermal model divides regions of the heat pipe into slices as shown in Fig. 1. The model determines the direction of the phase change in a slice by comparing the slice (wall) and vapor temperatures. If the superheat ($T_w - T_v$) is positive, evaporation takes place and the slice is a part of the evaporator; otherwise, it belongs to the condenser. This modeling strategy is applicable for all wick types. The axial heat conduction is accounted for by including the pertinent thermal resistances (R_{ax}) along the axial direction. The transverse heat transfer is modeled inserting the thermal resistances, which are specific to the evaporator (R_e) and condenser (R_c) regions. In what follows, the derivation of region specific thermal resistances is performed for the wick structure with rectangular grooves, as an example. The extension of the thermal model for sintered wicks is provided in Appendix B.

Figure 2 shows the transverse thermal resistance network on an arbitrary cross-section in the evaporator. The network is established between the base temperature (T_b^e) and the vapor temperature (T_v). It includes resistances due to heat conduction in both solid and liquid, and the phase change on the liquid-vapor interface. Since a considerable amount of evaporation originates from a micro-scale thin film region near the contact line (Akkus *et al.* 2017), the resolution of the solution should be increased in this region. Accordingly, the interfacial heat transfer is handled in two regions: (i) thin film region (the resistance associated with this region is R_{tf}^e) and (ii) intrinsic meniscus region (the resistance associated with this region is R_{gf}^e). In the actual case, 2D heat transfer takes places throughout the cross-section. The current approach, on the other hand, considers a 1D transfer of heat in two parallel routes by ignoring the 2-dimensionality of the problem. This is a reasonable approach considering the thickness of the liquid films in these regions. Thin film and meniscus regions are divided into $p-$ and $q-$ slices. The details of these regions are illustrated in Fig. 2B. The circuit representation of transverse thermal resistances in the evaporator together with the definition of each thermal resistance are

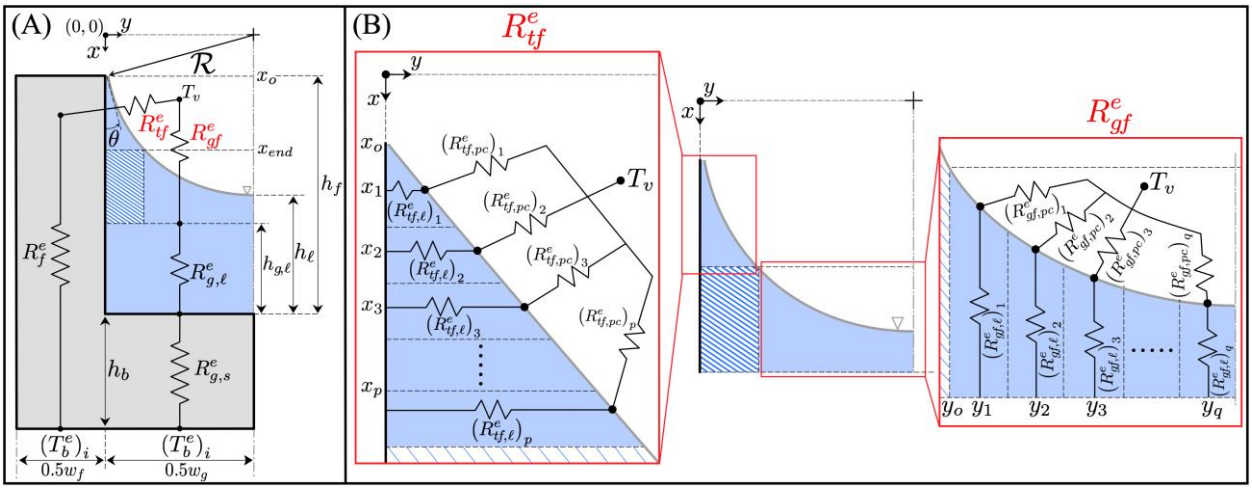

Figure 2. (A) Outline of transverse thermal resistance network in the evaporator. (B) Detailed view of thermal resistance network in thin film and intrinsic meniscus regions

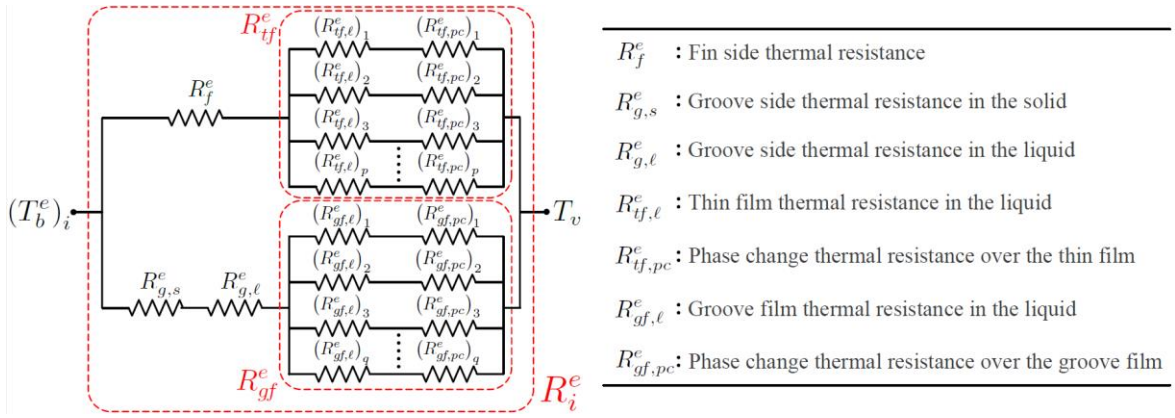

Figure 3. Circuit representation and the list of transverse thermal resistances in the evaporator

presented in Fig. 3. Formulations of these thermal resistances are provided in Appendix A.1.

Figure 4 shows the transverse thermal resistance network on an arbitrary cross-section in the condenser. Structure of the network is similar to that in the evaporator, but the thin film region expands on the fin top, where the majority of the condensation occurs (Akdag *et al.* 2019). This region is resolved by a denser thermal resistance network, whose details are illustrated in Fig. 4B. While the shape of the interface is defined as a circular meniscus in the evaporator, the film profile (on the fin top) in the condenser is determined based on a 4^{th} order polynomial (Do *et al.* 2008). The circuit representation of transverse thermal resistances in the condenser together with the definition of each thermal resistance are presented in Fig. 5. Formulations of these thermal resistances are provided in Appendix A.1.

The phase change process at the liquid-vapor interface induces a pertinent thermal resistance. This resistance depends on the rate of the phase change and the interfacial temperature difference. Relations derived from the kinetic theory of gases have been widely utilized in the estimation of phase change rates. Among them Schrage relation (Schrage, 1953) has been widely used because of its ability to successfully predict the rates during non-equilibrium phase change processes (Akkus *et al.* 2021). When the interfacial temperature difference is small, the approximate Schrage relation reduces to a popular form (Sujanani and Wayner Jr., 1991) that depends on the interfacial temperature and pressure jumps:

$$\dot{m}''_{pc} = a(T_{lv} - T_v) + b(p_v - p_l) \tag{2.6}$$

where

$$a = \frac{2\hat{\sigma}}{2-\hat{\sigma}}\left(\frac{M}{2\pi R_u T_{lv}}\right)^{1/2}\left(\frac{M p_v h_{fg}}{R_u T_v T_{lv}}\right) \tag{2.7a}$$

$$b = \frac{2\hat{\sigma}}{2-\hat{\sigma}}\left(\frac{M}{2\pi R_u T_{lv}}\right)^{1/2}\left(\frac{p_v V_l}{R_u T_{lv}}\right) \tag{2.7b}$$

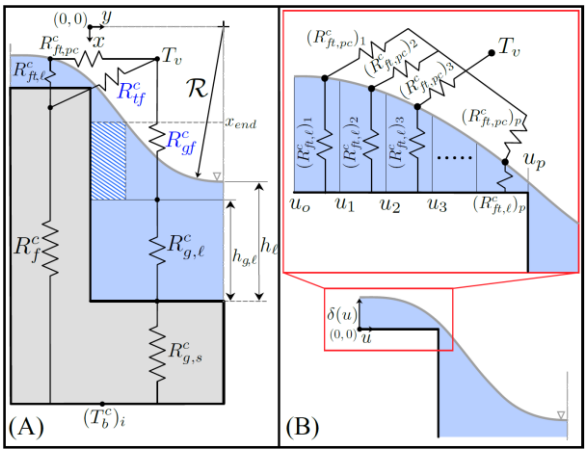

Figure 4. (A) Outline of transverse thermal resistance network in the condenser. (B) Detailed thermal resistance network in thin film (on the fin top) and intrinsic meniscus regions.

where R_u, M, and $\hat{\sigma}$ are universal gas constant, molar mass, and accommodation coefficient (taken as unity), respectively. Moreover, h_{fg} and V_l are latent heat of vaporization and molar volume of the fluid, respectively; and including those, all the fluid properties are evaluated at the vapor temperature in both thermal and fluid models. The pressure jump term in Eqn. (2.6) becomes effective when the variation of curvature and/or the effect of disjoining pressure are included. In the scope of this work, a detailed modeling of evaporating contact line is not performed, therefore the effect of pressure jump term is not accounted for. By negating this term, the interfacial phase change resistance can be written as follows:

$$(R^*_{\dots pc})_i = \frac{1}{a h_{fg} s_i L_i} \tag{2.8}$$

where s_i and L_i are the arc length of the interface and axial length of the slice, respectively. While the superscript $(*)$ stands for the evaporator or condenser, the subscript $(\dots, pc)$ denotes the location of the phase changing interface in the corresponding cross-section.

It should be noted that, unlike other capillary limit analysis in the literature which utilize simpler models, the multidimensional nature of HPAT necessitates the

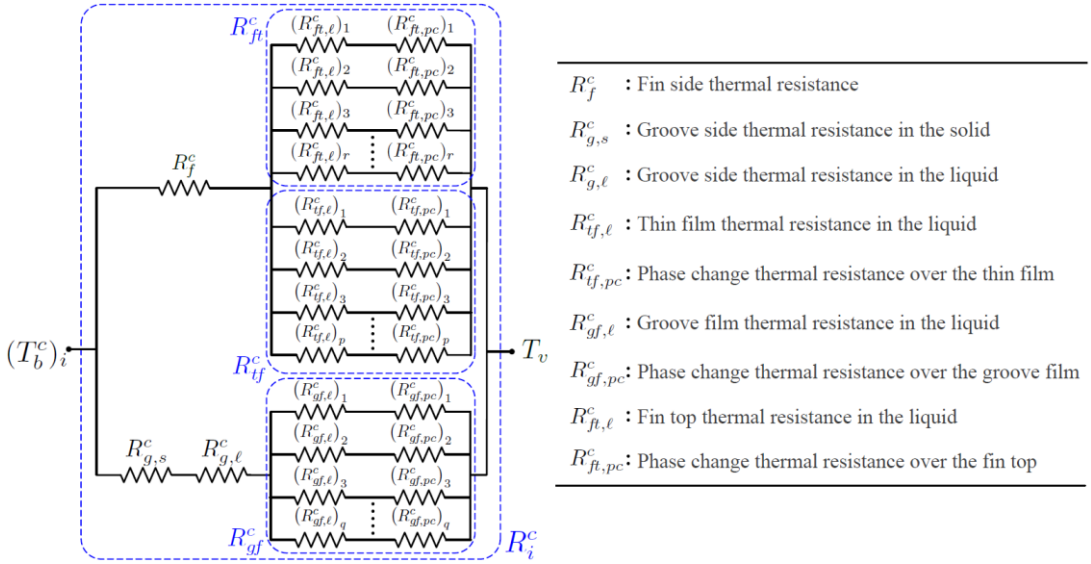

Figure 5. Circuit representation and the list of transverse thermal resistances in the condenser.

presence of several thermal resistances in the thermal network for a more realistic simulation of the inherently complex thermal phenomena. Several parameters, including the axial location, affect the magnitude of the resistances; and dominant paths of heat flow along the wick axis may change due to the changing magnitude of thermal resistances. Depending on the groove dimensions and edge angles, at a particular location, thin-film region thermal resistance may be at a minimum, creating a favorable path for heat flow, particularly on the evaporator side. Similarly, depending on the groove width, groove height and the thermal conductivity of the solid, the fin side and groove side thermal resistances in the solid may be negligible compared to other resistances in the thermal circuit. The fast computation ability of HPAT enables the inclusion of the entire network of resistances in the analysis, the relative significance of which can only be identified at a post processing step.

Solution Procedure

The iterative solution procedure is presented in Fig. 6. The lengths of the heat source length (L_e), adiabatic region (L_a) and heat sink (L_c), the details of the wick structure, the cooling condition at the heat sink (R^{conv} and T_∞) or alternatively a constant outer wall (base) temperature (T_c^b) and total heat input from the heat source (q_{tot}) are input parameters for the numerical model. For a given geometry and heat input, the phase change heat transfer (q_{pc}) and vapor temperature (T_v) are initially estimated. First, the flow model is utilized to determine the effective flow length (L^{eff}) and edge angle variation along the heat pipe ($\theta(z)$) (i.e. $\mathcal{R}(z)$). The resolution of the flow solution is determined by adjusting the number of slices in the axial direction, which can be set independently in each region. Second, the thermal model is utilized to determine q_{pc}, T_v, and the temperature distribution along the heat pipe. Similar to the flow model, the resolution is determined by adjusting the

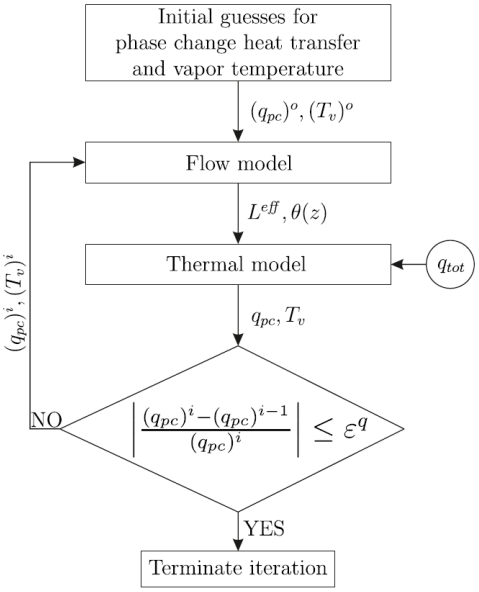

Figure 6. Solution algorithm

number of slices in the axial direction (see Fig. 1). Moreover, the frequency of slices utilized in resolving the phase change process on the liquid films is adjusted to ensure grid independence (see Fig. 2B and Fig. 4B). Finally, the calculated q_{pc} is compared against the estimates at the beginning of the loop. If the convergence criterion on q_{pc} is satisfied, the computation is terminated. Otherwise, q_{pc} and T_v are updated. Solution procedure is repeated until the convergence criterion is satisfied.

In the algorithm laid out in Fig. 6 the vapor temperature is needed for the calculation of the thermo-physical properties and phase change resistances, and during the iterations it is back calculated upon the solution of the thermal resistance circuit. This is a distinctive feature of

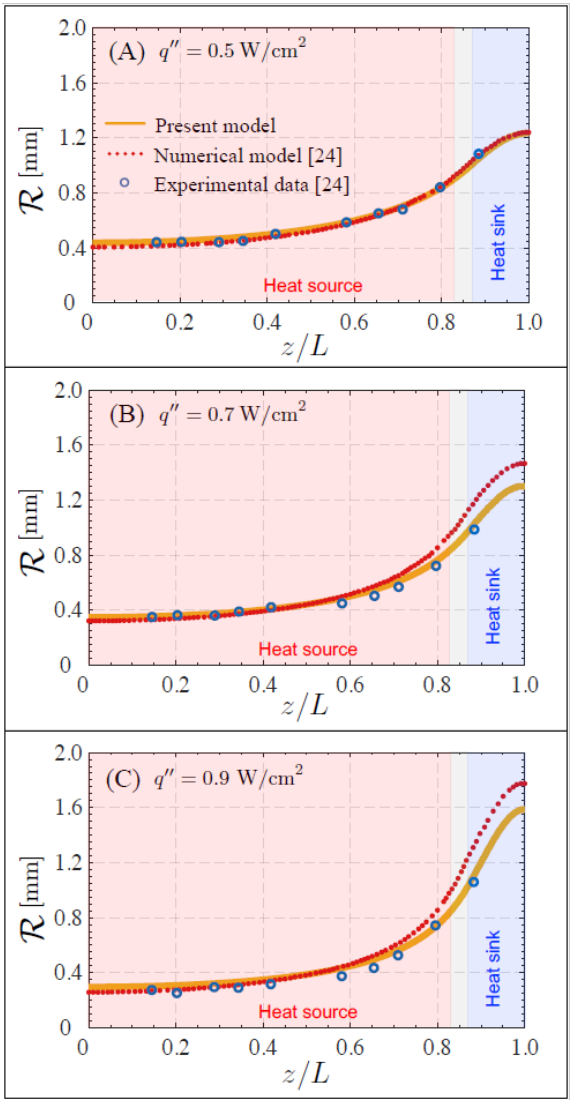

Figure 7. Radius of curvature variation along the heat pipe for heat loads (A) $q'' = 0.5\ \mathrm{W/cm^2}$, (B) $q'' = 0.7\ \mathrm{W/cm^2}$ and (C) $q'' = 0.9\ \mathrm{W/cm^2}$. Blue dots and red dotted lines indicate the experimental and numerical results of Lefèvre *et al.* (2008), respectively. Yellow lines show the predictions of H-PAT.

the current solution algorithm, since other models solving the differential equation form of the energy balance need to use the vapor temperature as a boundary condition, hence requiring the convergence of the vapor temperature for the convergence of the combined heat transfer/fluid flow/phase change/interface shape problem. In the current approach, the necessity of using the vapor temperature as a boundary condition is avoided, which results in a faster solution of the iterative process. This is why the convergence of the solution is checked based on the convergence of phase change heat fluxes, q_{pc}, rather than the vapor temperature, T_v.

RESULT AND DISCUSSION

Validation of the Flow Model

The flow model basically determines the variation of the meniscus shape. The performance of the present flow model can be evaluated by comparing its predictions with the previous experimental measurements. To this effect, two past works, which utilized rectangular grooved wicks with constant (Lefèvre *et al.*, 2008) and varying (Lefèvre *et al.*, 2010) cross-sections along the groove axis, are selected for the validation of the flow model. Both studies reported the variation of the radius of curvature of the meniscus along the groove axis measured by confocal microscopy. The details of the heat pipe configurations utilized in Refs. (Lefèvre *et al.*, 2008) and (Lefèvre *et al.*, 2010) are provided in Table 1 (please see Fig. 12 for the geometric parameters).

Former study (with constant cross-section) (Lefèvre *et al.*, 2008) was conducted for three different heat fluxes: $0.5\ \mathrm{W/cm^2}$, $0.7\ \mathrm{W/cm^2}$ and $0.9\ \mathrm{W/cm^2}$. In addition to the measurement of meniscus curvature, a comprehensive 3D numerical model was also developed in (Lefèvre *et al.*, 2008) by solving the mass and momentum equations in both liquid and vapor domains together with Young-Laplace equation and a multi-directional thermal resistance network. Using the same geometry and conditions (see Table 1), the experiments are simulated by H-PAT. In order to match the vapor (working) temperature kept constant at the experiments, the cooling conditions at the heat sink are adjusted in H-PAT similar to the practice adopted in the experiments. The experimental and numerical findings of (Lefèvre *et al.*, 2008) are compared with the predictions of H-PAT in Fig. 7. Results show that the radius of curvature estimates of H-PAT along the heat pipe are in excellent agreement with the experiments. The predictions of comprehensive numerical model developed in (Lefèvre *et al.*, 2008) deviate with increasing heat loads, whereas H-PAT matches the experiments for all heat loads applied.

H-PAT has the ability to simulate wicks with variable flow area by defining the variation of wick dimensions as a function of the axial direction (see Eq. 2.5). In order to assess its computational performance on the rectangular grooves with variable cross-section area, H-PAT is utilized to simulate a pertinent previous experiment (Lefèvre *et al.*, 2010), where the groove width varied linearly (see Fig. 8A), $i.e. w(z) = w_1 + w_2(z)$. The constants w_1 and w_2 are calculated as 1.1×10^{-4}[m] and 2.43×10^{-2}, respectively, for the groove geometry in (Lefèvre *et al.*, 2010).

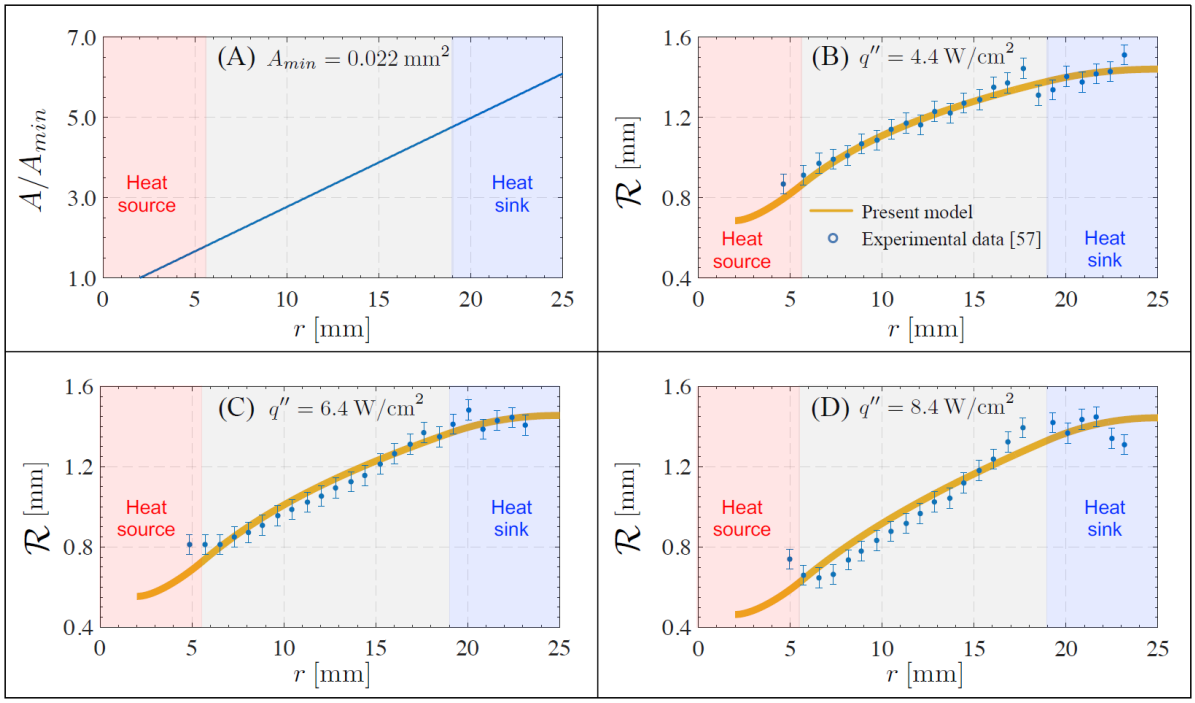

Figure 8. (A) Variation of cross-sectional groove area and radius of curvature along the flow axis for the heat loads: (B) $q'' = 4.4\ \mathrm{W/cm^2}$, (C) $q'' = 6.4\ \mathrm{W/cm^2}$ and (D) $q'' = 0.5\ \mathrm{W/cm^2}$. Blue dots are experimental results of Lefèvre *et al.* (2010). Yellow lines are the predictions of H-PAT.

Although five different heat loads were applied, the radius of curvature variation along the heat pipe was significant only for the highest three heat loads ($4.4\ \mathrm{W/cm^2}$, $6.4\ \mathrm{W/cm^2}$ and $8.4\ \mathrm{W/cm^2}$). Vapor temperature was kept constant at 30°C for all heat uxes. The experimental measurements of the radius of curvature in (Lefèvre *et al.*, 2010) are compared against the predictions of H-PAT in Figs. 8B-D. The results show that for the majority of the experimental results, the predictions of H-PAT match the experiments within the uncertainty of measurements, the match being particularly good in the adiabatic region. Small deviations near the evaporator end can be attributed to the transition of the wick geometry from a grooved to a pillar structure at the evaporator in the experiment. To the best of authors' knowledge, the numerical validation of the experiments in (Lefèvre *et al.*, 2010) is performed for the first time owing to the capability of H-PAT in handling wicks with varying cross-sectional flow area.

Validation of Thermal Model

The output of the thermal model is the temperature distribution along the heat pipe which can be used to determine the effective thermal resistance (or effective thermal conductivity) of a heat pipe subjected to a certain heat load. As a first attempt for the validation of thermal model, H-PAT is exercised to simulate the experiments conducted on the heat pipes with rectangular grooves in (Hopkins *et al.*, 1999), where the experiments were conducted for 15 different heat loads between 3.0 and 127 W, and the effective thermal resistances were reported for each case.

Likewise, utilizing the same geometry and conditions (see Table 1), H-PAT calculates the effective thermal resistance by dividing the temperature difference between the two ends to the total heat input. As shown in Fig. 9, there is an excellent match between the predictions of the current model and the experimental results in (Hopkins *et al.*, 1999) across a wide range of heat loads. Hopkins et al., (1999) attributed their decreasing thermal resistances with heat loads to the thinning liquid film at the evaporator. In essence, the liquid distribution is adjusted along the entire groove such that the liquid film may become thicker or form a liquid pool near the condenser end, while it becomes thinner at the evaporator. H-PAT is able to catch these variations, and accordingly, it is successful in capturing the converging pattern of resistance with heat loads up to the onset of dryout.

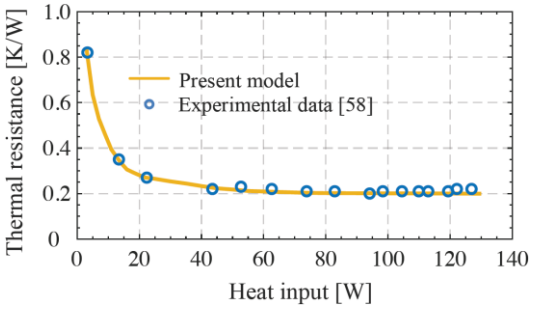

Figure 9. Variation of thermal resistance with heat load. Blue circles are the experimental results of Hopkins *et al.* (1999). Yellow line shows the predictions of H-PAT.

As a second attempt, the performance of H-PAT is assessed by conducting a benchmark experiment on a at plate heat pipe setup constructed for the current study. The experimental heat pipe assembly consists of five parts, namely main frame, grooved base plate, transparent top cover, heat source, and heat sink (see Fig. 10). In the experimental setup Edward RV3 two stage rotary vane pumps, Agilent 34972A data acquisition/data logger switch unit, Thermo/Neslab digital refrigerated bath circulator ($\mp 0.01℃$), Omega T-type thermocouple ($\mp 0.5℃$) were used. This modular structure enables testing wicks with different geometries and materials by simply changing the grooved base plate, which was aluminum for this particular experiment set. T-type thermocouples were placed inside the holes machined at the bottom of the groove frame. Transparent top cover is manufactured from acrylic to enable a clear visualization of the groove frame. Sealing between the main and top frames as well as that with the main and grooved base plate were secured by vacuum grade o-rings. Moreover, the heat sources and heat sinks with different sizes/geometries can be interchangeably utilized in this setup. At the beginning of the experiment, the heat pipe was filled with the working fluid, IPA. Then, the heat pipe was operated under the heat load of 2.1 W/cm^2 until steady state was reached. Following this, an incremental amount of IPA was aspirated from the heat pipe and testing was commenced. This procedure was repeated until no IPA remains in the heat pipe. The temperature data was recorded throughout the entire test. The point with minimum temperature difference was obtained from these experiments was accepted as the optimum working point of the heat pipe. The parameters and working conditions, the experiment is also simulated by H-PAT for the operating condition corresponding to the optimum point. Predictions of H-PAT are compared with experimental wall temperature measurements for

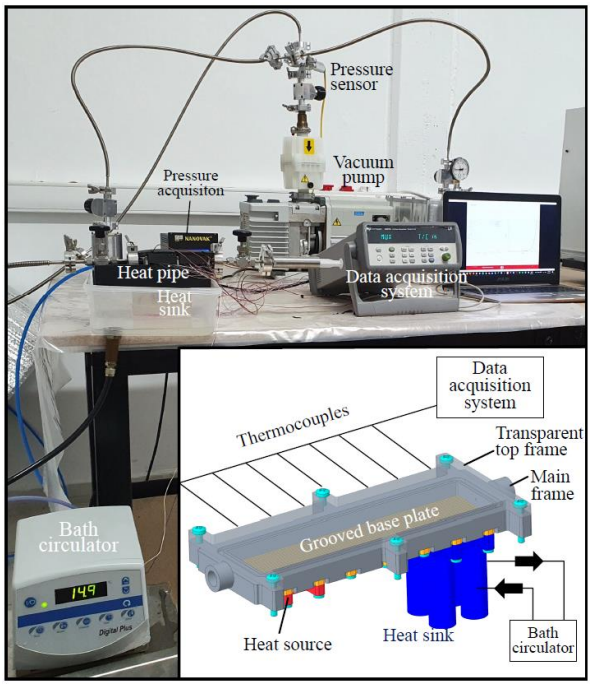

Figure 10. Experimental setup

both heat pipes in Fig. 11. As shown, the thermal model successfully captures the temperature variation along both heat pipes. Slightly overestimated temperatures near the heat source of the heat pipe with smaller grooves might be attributed to parasitic experiments were conducted for two different heat pipes (geometries given in Table 1). Utilizing the same geometrical heat loss to the ambient, although insulation was applied in every experiments. As shown in Fig. 11, H-PAT is able to provide vapor temperature, which can be viewed as the working temperature of the heat pipe. Intersection of

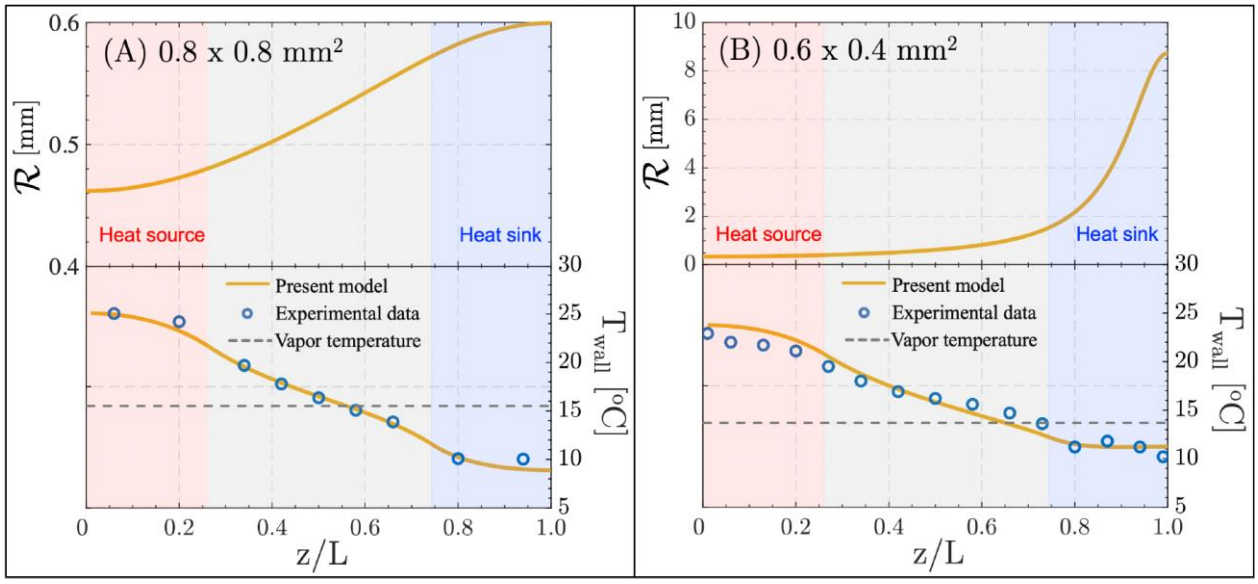

Figure 11. Variation of wall temperature along the heat pipe. Blue circles are experimental results and experimental uncertainty is smaller than the size of the circles. Yellow solid and gray dashed lines shows the wall temperature and vapor temperature predictions of H-PAT, respectively.

vapor temperature and wall temperature marks the point of transition between evaporator and condenser sections.

As demonstrated by preceding validations, H-PAT is highly successful in simulating the operation of a heat pipe working for different heat loads. Moreover, the simulation time is fast (in the order of seconds) owing to its unique solution approach that accounts for the all geometric variations in both wick structure and liquid film profile in the construction of thermal model, but avoids the solution of particular thin film phase change models by specifying and iterating the axial mass flow rate in the flow model, which eliminates the need for solving a multi-dimensional flow problem. This approach enables the prediction of the amount of overall heat transfer via phase change together with vapor temperature. Considering its accuracy along with fast computation, H-PAT positions itself not only as a diagnostic tool, but also as a design tool that can be confidently utilized by thermal design engineers in iterative design processes.

CONCLUDING REMARKS AND OUTLOOK

Heat Pipe Analysis Toolbox, in short H-PAT, is a fast diagnosis and design toolbox for the simulation of heat pipes. H-PAT can predict the fluid flow and heat transfer in a heat pipe under varying heat inputs up to the onset of dryout. In other words, H-PAT captures the capillary limit of the heat pipe, whereas sonic, entrainment, and viscous (vapor pressure) limits are not taken into consideration in the current version, which does not include vapor zone in its solution domain. In addition, boiling heat transfer is not covered by H-PAT based on the assumption of bubble-free evaporation throughout the evaporator. Adaptable structure of H-PAT allows the simulation of heat pipes with different wick structures. A heat pipe responds to heat input changes by simply varying the liquid distribution along the wick. H-PAT is able to capture these variations including the rarely considered pool region in the condenser. Reliability of H-PAT is proved with benchmark simulations for rectangular grooves with both constant and variable cross-section along the heat pipe. The latter remarks a distinctive feature reflecting the potential of H-PAT in the assessment of heat pipes having wicks with varying topology.

Because of its high accuracy and fast computation together with a user friendly interface, H-PAT is a candidate for frequent use by researchers and design engineers in the field of thermal management, and available via MathWorks File Exchange. Although its accuracy and fast computation, H-PAT has some restrictions. First and fore-most, it requires the analytical solutions and/or correlations for the liquid flow along the wick, which may not be available for unconventional complex geometries. Moreover, skipping the solution of detailed thin film phase change models may prevent obtaining the precise variation of the liquid film at a cross-section due to the absence of near wall effects such as dispersion and structural components of disjoining pressure (Akdag *et al.*, 2020; Setchi *et al.*, 2019). In addition, in its current form, H-PAT does not solve the vapor flow, thereby neglecting the associated viscous losses, and assumes uniform vapor properties along the heat pipe. Despite its negligible role in the benchmark studies considered in this work, resolving vapor flow may be crucial in certain heat pipe applications, especially in the case of thin heat pipes with small vapor spacing. Finally, operation with partial dryout is not considered in the current version of H-PAT. In the light of these our future research efforts will focus on adding the following features to H-PAT: the inclusion of vapor flow and porous wick structures, and simulation in the presence of partial dryout.

ACKNOWLEDGEMENTS

S.S. acknowledges the support provided by Scientific and Technological Research Council of Turkey (TÜBİTAK) through Science Fellowships and Grant Programmes (BİDEB 2211). B.Ç. would like to acknowledge the funding from the Turkish Academy of Sciences through Outstanding Young Scientist Program (TÜBA-GEBİP) and The Science Academy, Turkey through Distinguished Young Scientist Award (BAGEP).

DECLARATIONS OF INTEREST

None.

APPENDIX A. Formulation of Thermal Resistances in Grooved Wicks

Formulations of thermal resistances utilized in the both evaporator and the condenser are listed below. Note that the superscript (*) in the following equations is replaced with “e” for the evaporator and “c” for the condenser.

$$R_f^* = \frac{h_b + h_g - 0.5(x_{end} - x_0)}{k_s(0.5w_f)L_i} \tag{A.1}$$

$$R_{g,s}^* = \frac{h_b}{k_s(0.5w_g)L_i} \tag{A.2}$$

$$R_{g,l}^* = \frac{h_{g,l}}{k_l(0.5w_g)L_i} \tag{A.3}$$

$$(R_{tf,l}^*)_n = \frac{\bar{\delta}_n}{k_l(x_n - x_{n-1})L_i} \tag{A.4}$$

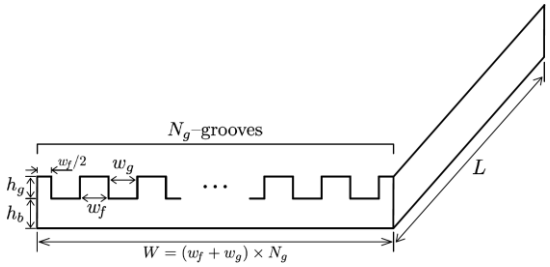

Figure 12. Grooved heat pipe

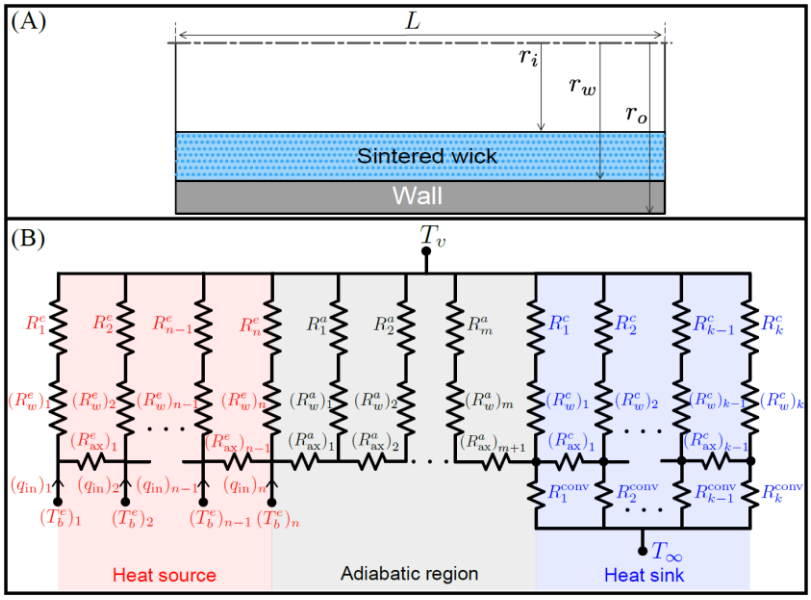

Figure 13. Cylindrical sintered wick heat pipe

$$(R^*_{tf,pc})_n = \frac{1}{a h_{fg} (s_n - s_{n-1}) L_i} \tag{A.5}$$

$$(R^*_{gf,l})_n = \frac{\bar{\delta}_{g,n}}{k_l (y_n - y_{n-1}) L_i} \tag{A.6}$$

$$(R^*_{gf,pc})_n = \frac{1}{a h_{fg} (s_{g,n} - s_{g,n-1}) L_i} \tag{A.7}$$

where h_{fg} is the latent heat of vaporization, k_s, k_l, and k_w are the thermal conductivity of the wall material, working liquid, and wick structure, respectively. All the geometric parameters are shown in Fig. 12. In addition to these resistances, the fin top resistances due to condensation of the liquid at the condenser occur and formulated as:

$$(R^c_{ft,l})_n = \frac{\bar{\delta}_n}{k_l (u_n - u_{n-1}) L_i} \tag{A.8}$$

$$(R^*_{ft,pc})_n = \frac{1}{a h_{fg} (s_{ft,n} - s_{ft,n-1}) L_i} \tag{A.9}$$

Finally, overall resistances for evaporating and condensing cross-sections are:

$$R^e = \left[\frac{1}{R^e_{fb} + R^e_f + R^e_{tf}} + \frac{1}{R^e_{gb} + R^e_{g,l} + R^e_{gf}} \right]^{-1} \tag{A.10}$$

$$R^c = \left[\frac{1}{R^c_{fb} + R^c_f + (1/R^c_{tf} + 1/R^c_{ft})} + \frac{1}{R^c_{gb} + R^c_{g,l} + R^c_{gf}} \right]^{-1} \tag{A.11}$$

APPENDIX B. Extension of the Model for Sintered Wicks

In this section, the extension of the fluid flow and thermal models are given for cylindrical heat pipes with sintered wicks. A relation between mass flow rate of the liquid and the pressure variation along the heat pipe for sintered wicks can be written using Darcy equation:

$$U_m = \frac{\kappa}{\mu_l} \frac{\Delta P}{L^{eff}} \tag{B.1}$$

$$A_{wick} = \pi (r_w^2 - r_i^2) \tag{B.2}$$

where κ is the permeability, and the r_i and r_w are the corresponding radius values shown in Fig. 13A. The pressure distribution equation for the liquid can be obtained by combining mass flow rate prediction along the heat pipe with the mass flow rate equation as follows:

$$p(z) = \int \left(\frac{\dot{m}_l}{\mathbb{G}(z)} - f_b \right) dz, \quad 0 \le z \le L^{eff} \tag{B.3}$$

where

$$\mathbb{G}(z) = \frac{\nu_l}{\kappa \pi A_{wick}} \tag{B.4}$$

where ν_l kinematic viscosity of the liquid. It should be noted that geometric function, $\mathbb{G}$, is not the function of axial distance due to the assumption of constant flow area. Formulations of the resistances forming the thermal resistance network are shown in Fig. 13B are as follows:

$$(R_w^*)_i = \frac{\ln(r_o/r_w)}{2\pi k_s L_i} \quad \text{(B.5)}$$

$$R_l^* = \frac{\ln(r_w/r_i)}{2\pi k_{eff} L_i} \quad \text{(B.6)}$$

$$(R_{ax}^*)_i = \frac{L_i}{\pi[k_s(r_o^2 - r_w^2) + k_{eff}(r_w^2 - r_i^2)]} \quad \text{(B.7)}$$

where effective thermal conductivity of the porous wick structure can be defined as:

$$k_{eff} = k_w \frac{[2 + (k_l/k_w) - 2\varepsilon(1 - k_l/k_w)]}{[2 + (k_l/k_w) + \varepsilon(1 - k_l/k_w)]} \quad \text{(B.8)}$$

where ε is the porosity of the wick, k_s, k_l, and k_w are the thermal conductivity of the wall material, working liquid, and wick structure, respectively.

REFERENCES

Aghvami M. and Faghri A., 2011, Analysis of flat heat pipes with various heating and cooling configurations. *Appl. Therm. Eng.*, 31(14-15):2645-2655.

Akdag O., Akkus Y., and Dursunkaya Z., 2019, The effect of disjoining pressure on the shape of condensing films in a fin-groove corner. *Int. J. Therm. Sci.*, 142:357-365.

Akdag O., Akkus Y., and Dursunkaya Z., 2020, On the effect of structural forces on a condensing film profile near a fin-groove corner. *Int. Commun. Heat Mass*, 116:104686.

Akkus Y. and Dursunkaya Z., 2016, A new approach to thin film evaporation modeling. *Int. J. Heat Mass Tran.*, 101:742-748.

Akkus Y., Gurer A. T., and Bellur K., 2021, Drifting mass accommodation coefficients: *in situ* measurements from a steady state molecular dynamics setup. *Nanosc. Microsc. Therm.*, 25(1):25-45.

Akkus Y., Nguyen C. T., Celebi A. T., and Beskok A., 2019, A first look at the performance of nano-grooved heat pipes. *Int. J. Heat Mass Tran.*, 132:280-287.

Akkus Y., Tarman H. I., Çetin B., and Dursunkaya Z., 2017, Two-dimensional computational modeling of thin film evaporation. *Int. J. Therm. Sci.*, 121:237-248.

Alijani H., Cetin B., Akkus Y., and Dursunkaya Z., 2018, Effect of design and operating parameters on the thermal performance of flat grooved heat pipes. *Appl. Therm. Eng.*,132:174-187.

Alijani H., Cetin B., Akkus Y., and Dursunkaya Z., 2019, Experimental thermal performance characterization of flat grooved heat pipes. *Heat Transfer Eng.*, 40(9-10):784-793.

Anand A. R., Vedamurthy A. J., Chikkala S. R., Kumar S., Kumar D., and Gupta P. P., 2008, Analytical and experimental investigations on axially grooved aluminum-ethane heat pipe. *Heat Transfer Eng.*, 29(4):410-416.

Atay A., Sarıaslan B., Kuşcu Y. F., Saygan S., Akkus Y., Gürer A. T., Çetin B., and Dursunkaya Z., 2019, Performance assessment of commercial heat pipes with sintered and grooved wicks under natural convection. *J. Therm. Sci. Tech*., 39(2):101-110.

Babin B. R., Peterson G. P., and Wu D., 1990, Steady-state modeling and testing of a micro heat pipe. *J. Heat Transf.*, 112:595-601.

Catton I. and Yao Q., 2016, A designer fluid for aluminum phase change devices, Volume III Performance enhancement in copper heat pipes. *Technical report, University of California, Los Angeles, United States*.

Chang F. L. and Hung Y. M., 2014, The coupled effects of working fluid and solid wall on thermal performance of micro heat pipes. *Int. J. Heat Mass Tran.*, 73:76-87.

Chen Y., Zhang C., Shi M., Wu J., and Peterson G. P., 2009, Study on flow and heat transfer characteristics of heat pipe with axial "ω"-shaped microgrooves. *Int. J. Heat Mass Tran.*, 52(3-4):636-643.

Chi S. W., 1976, Heat Pipe Theory and Practice: A Sourcebook. *McGraw-Hill-Hemisphere Series in Fluids and Thermal Engineering. Hemisphere Publishing Corporation*.

Desai A. N., Singh V. K., and Patel R. N., 2019, Effect of geometrical parameters on the thermal performance of ammonia-based trapezoidal-shaped axial grooved heat pipe. *J. Heat Transf.*, 141(12).

Do K. H., Kim S. J., and Garimella S. V., 2008, A mathematical model for analyzing the thermal characteristics of a flat micro heat pipe with a grooved wick. *Int. J. Heat Mass Tran.*,51(19-20):4637-4650.

Elnaggar M. H. A., Abdullah M. Z., and Mujeebu M. A., 2012, Characterization of working fluid in vertically mounted finned u-shape twin heat pipe for electronic cooling. *Energy Convers. Manage.*, 62:31-39.

Faghri A., 1989, Performance characteristics of a concentric annular heat pipe: Part 2-vapor flow analysis. *J. Heat Transf.*, 111(4).

Faghri A., 1995, Heat Pipe Science and Technology. *Global Digital Press*.

Ferrandi C., Iorizzo F., Mameli M., Zinna S., and Marengo M., 2013, Lumped parameter model of sintered heat pipe: Transient numerical analysis and validation. *Appl. Therm. Eng.*, 50(1):1280-1290.

Grover G. M., Cotter T. P., and Erickson G. F., 1964, Structures of very high thermal conductance. *J. Appl. Phys.*, 35(6):1990-1991.

Hoa C., Demolder B., and Alexandre A., 2003, Roadmap for developing heat pipes for Alcatel space's satellites. *Appl. Therm. Eng.*, 23(9):1099-1108.

Hopkins R., Faghri A., and Khrustalev D., 1999, Flat miniature heat pipes with micro capillary grooves. *J. Heat Transf.*, 121(1):102-109.

Huang Y. and Chen Q., 2017, A numerical model for transient simulation of porous wicked heat pipes by lattice boltzmann method. *Int. J. Heat Mass Tran.*, 105:270-278.

Hung Y. M. and Tio K. K., 2010, Analysis of microheat pipes with axial conduction in the solid wall. *J. Heat Transf.*, 132(7).

Hung Y. M. and Tio K. K., 2012, Thermal analysis of optimally designed inclined micro heat pipes with axial solid wall conduction. *Int. Commun. Heat Mass*, 39(8):1146-1153.

Jafari D., Wits W. W., and Geurts B. J., 2020, Phase change heat transfer characteristics of an additively manufactured wick for heat pipe applications. *Appl. Therm. Eng.*, 168:114890.

Jiang L., Ling J., Jiang L., Tang Y., Li Y., Zhou W., and Gao J., 2014, Thermal performance of a novel porous crack composite wick heat pipe. *Energ. Convers. Manage.*, 81:10-18.

Khalili M. and Shafii M. B., 2016, Experimental and numerical investigation of the thermal performance of a novel sintered-wick heat pipe. *Appl. Therm. Eng.*, 94:59-75.

Khrustalev D. and Faghri A., 1994, Thermal analysis of a micro heat pipe. *J. Heat Transf.*, 116(1):189-198.

Khrustalev D. and Faghri A., 1995, Thermal characteristics of conventional and flat miniature axially grooved heat pipes. *J. Heat Transf.*, 117(4):1048-1054.

Kim S. J., Seo J. K., and Do K. H., 2003, Analytical and experimental investigation on the operational characteristics and the thermal optimization of a miniature heat pipe with a grooved wick structure. *Int. J. Heat Mass Tran.*, 46(11):2051-2063.

Kolliyil J., Yarramsetty N., and Balaji C., 2020, Numerical modeling of a wicked heat pipe using lumped parameter network incorporating the Marangoni effect. *Heat Transfer Eng.*, :1-15.

Lefèvre F., Rullière R., Lips S., and Bonjour J., 2010, Confocal microscopy for capillary film measurements in a flat plate heat pipe. *J. Heat Transf.*, 132(3).

Lefèvre F., Rullière R., Pandraud G., and Lallemand M., 2008, Prediction of the temperature field in flat plate heat pipes with micro-grooves–experimental validation. *Int. J. Heat Mass Tran.*, 51(15-16):4083-4094.

Li Y., He J., He H., Yan Y., Zeng Z., and Li B., 2015, Investigation of ultra-thin flattened heat pipes with sintered wick structure. *Appl. Therm. Eng.*, 86:106-118.

Lips S., Lefèvre F., and Bonjour J., 2011, Physical mechanisms involved in grooved flat heat pipes: experimental and numerical analyses. *Int. J. Therm. Sci.*, 50(7):1243-1252.

Longtin J. P., Badran B., and Gerner F. M., 1994, A one-dimensional model of a micro heat pipe during steady-state operation. *J. Heat Transf.*, 116:709-715.

Nilson R. H., Tchikanda S. W., Griffiths S. K., and Martinez M. J., 2006, Steady evaporating flow in rectangular microchannels. *Int. J. Heat Mass Tran.*, 49:1603-1618.

Odabaşı G., 2014, Modeling of multidimensional heat transfer in a rectangular grooved heat pipe. Ph.D. Thesis, Middle East Technical University.

Ömür C., Uygur A. B., Horuz İ., Işık H. G., Ayan S., and Konar M., 2018, Incorporation of manufacturing constraints into an algorithm for the determination of maximum heat transport capacity of extruded axially grooved heat pipes. *Int. J. Therm. Sci.*, 123:181-190.

Peterson G. P., 1994, An Introduction to Heat Pipes: Modeling, Testing, and Applications. *Wiley*.

Peterson G. P., Duncan A. B., and Weichold M. H., 1993, Experimental investigation of micro heat pipes fabricated in silicon wafers. *J. Heat Transf.*, 115(3):751-756.

Reay D., McGlen R., and Kew P., 2013, Heat Pipes: Theory, Design and Applications. *Butterworth-Heinemann*.

Rullière R., Lefèvre F., and Lallemand M., 2007, Prediction of the maximum heat transfer capability of two-phase heat spreaders–experimental validation. *Int. J. Heat Mass Tran.*, 50(7-8):1255-1262.

Schneider G. E. and DeVos R., 1980, Non-dimensional analysis for the heat transport capability of axially grooved heat pipes including liquid/vapor interaction. *In AIAA*, page 214.

Schrage R.W., 1953, A Theoretical Study of Interphase Mass Transfer. *Columbia University Press, New York*.

Setchi A., Chen Y., Yu J., and Wang H., 2019, Structural effects in partially-wetting thin evaporating liquid films near the contact line. *Int. J. Heat Mass Tran.*, 132:420-430.

Singh M., 2020, Capillarity enhancement of micro heat pipes using grooves with variable apex angle. *Int. J. Therm. Sci.*, 150:106239.

Sujanani M. and Wayner P.C., 1991, Microcomputer-enhanced optical investigation of transport processes with phase change in near-equilibrium thin liquid films. *J. Colloid Interf. Sci.*, 2:472-488.

Suman B., De S., and DasGupta S., 2005, A model of the capillary limit of a micro heat pipe and prediction of the dry-out length. *Int. J. Heat Fluid Fl.*, 26(3):495-505.

Tio K. K. and Hung Y. M., 2015, Analysis of overloaded micro heat pipes: Effects of solid thermal conductivity. *Int. J. Heat Mass Tran.*, 81:737-749.

Vafai K., 1984, Convective flow and heat transfer in variable-porosity media. *J. Fluid Mech.*, 147:233-259.

Vafai K. and Tien C. L., 1981, Boundary and inertia effects on flow and heat transfer in porous media. *Int. J. Heat Mass Tran.*, 24(2):195-203.

Vafai K. and Wang W., 1992 Analysis of flow and heat transfer characteristics of an asymmetrical flat plate heat pipe. *Int. J. Heat Mass Tran.*, 35(9):2087-2099.

Zhu N. and Vafai K., 1999, Analysis of cylindrical heat pipes incorporating the effects of liquid-vapor coupling and non-darcian transport-a closed form solution. *Int. J. Heat Mass Tran.*,42(18):3405-3418.

Zhu N. and Vafai K., 1996, The effects of liquid-vapor coupling and non-Darcian transport on asymmetrical disk-shaped heat pipes. *Int. J. Heat Mass Tran.*, 39(10):2095-2113.